Geophysical Research Letters

RESEARCH LETTER
10.1029/2022GL101035

Subsurface Ocean Temperature Responses to the Anthropogenic Aerosol Forcing in the North Pacific

Jia-Rui Shi[1], **Young-Oh Kwon**[1], **and Susan E. Wijffels**[1]

[1]Woods Hole Oceanographic Institution, Woods Hole, MA, USA

Key Points:

- A pattern recognition method is applied to extract aerosol-induced subsurface temperature pattern from internal variability in North Pacific
- Based on two large-ensemble simulations, aerosols govern a nonmonotonic feature in temperature change with a characteristic pattern
- This spatiotemporal feature can be obtained from observations since 1950, although there are some differences with the modeled results

Supporting Information:

Supporting Information may be found in the online version of this article.

Correspondence to:

J.-R. Shi,
jia-rui.shi@whoi.edu

Citation:

Shi, J.-R., Kwon, Y.-O., & Wijffels, S. E. (2023). Subsurface ocean temperature responses to the anthropogenic aerosol forcing in the North Pacific. *Geophysical Research Letters*, *50*, e2022GL101035. https://doi.org/10.1029/2022GL101035

Received 26 AUG 2022
Accepted 5 JAN 2023

Author Contributions:

Conceptualization: Jia-Rui Shi
Formal analysis: Jia-Rui Shi
Investigation: Jia-Rui Shi
Supervision: Young-Oh Kwon, Susan E. Wijffels
Writing – original draft: Jia-Rui Shi
Writing – review & editing: Jia-Rui Shi, Young-Oh Kwon, Susan E. Wijffels

Abstract Separating the climate response to external forcing from internal climate variability is a key challenge. While most previous studies have focused on surface responses, here we examine zonal-mean patterns of North Pacific subsurface temperature responses. In particular, the changes since 1950 driven by anthropogenic aerosol emissions are found by using a pattern recognition method. Based on the single-forcing large-ensemble simulations from two models, we show that aerosol forcing caused a nonmonotonic temporal response and a characteristic zonal-mean pattern within North Pacific, which is distinct from the pattern associated with internal variability. The aerosol-forced pattern with the nonmonotonic temporal feature shows a substantial temperature change in subpolar regions and a reversed change on the southern flank of the subtropical gyre. A similar characteristic pattern and nonmonotonic time evolution are extracted from the subsurface observations, which likely reflect the subsurface responses to the aerosol forcing, although differences exist with the simulated responses.

Plain Language Summary Pacific climate has long been of interest as considerable evidence has emerged of a decades-long change. As the background noise, such as Interdecadal Pacific Oscillation and El Niño-Southern Oscillation, is very strong in the Pacific, it remains a major challenge to detect and understand the changes due to human activities. In this study, we take advantage of a pattern recognition method to investigate the North Pacific subsurface temperature response to aerosol emissions, a suspension of fine particles in air, due to industrial development. The results are primarily based on two sets of model simulations with different phases of background noise and identical external forcing, which stems from anthropogenic aerosol emissions only. We find that the aerosol emissions from North America and Europe cause a clear nonmonotonic time evolution (increased during 1950–1985 and then decreased afterward) and a characteristic zonal mean pattern of the subsurface ocean temperature within the North Pacific. The extracted temporal and spatial features from ocean observations are broadly consistent with those from models, although there are some differences.

1. Introduction

Climate variations in the Pacific have long been of interest as considerable evidence has emerged of a decades-long change in the Pacific atmosphere and ocean. Superimposed on a long-term trend in sea surface temperatures, the Pacific climate is substantially affected by its large internal variability, that is, Interdecadal Pacific Oscillation and El Niño-Southern Oscillation. Due to the large size of the Pacific basin, these prominent modes of Pacific climate variability modulate the global mean surface temperature, such as the warming "hiatus" between 1998 and 2012 (Dai et al., 2015; England et al., 2014; Kosaka & Xie, 2013; Meehl et al., 2016; Trenberth & Fasullo, 2013).

Given this background of strong internal variability, isolating the Pacific response to anthropogenic climate change has been a major challenge. Greenhouse gases (GHGs) and anthropogenic aerosols (AAs) are both important radiative forcing agents that drive global and regional climate change. On a global scale, AA forcing can partly compensate for the warming induced by GHGs (Bonfils et al., 2020; Irving et al., 2019; Shi et al., 2018; Wang et al., 2016), which increases the difficulty of separating these forced signals. Post-World War II there was a large increase in aerosol emissions. It has been found that AAs can give rise to the cooling in the global mean surface temperature (Smith et al., 2016; Stott et al., 2000; Wilcox et al., 2013). From the energetic perspective, AAs concentrated in Northern Hemisphere (NH) can lead to a hemispheric energy imbalance which has been shown to drive a southward shift of the Inter-Tropical Convergence Zone and Hadley Cells (Chung & Soden, 2017; Hwang & Frierson, 2013). Moreover, the emissions of AAs during the historical period are nonmonotonic in time and

non-uniform across the globe, which can give rise to characteristic forced spatial patterns at the surface (Deser et al., 2020; Shi et al., 2022). An intensification of Pacific trade winds, Walker circulation, and wind-driven ocean circulation is found to be partially attributed to AA forcing since the 1990s (Allen et al., 2014; England et al., 2014; Takahashi & Watanabe, 2016). In contrast, Oudar et al. (2018) found that the observed global cooling in the early 21st century is attributable to internal variability, and the intensified trade winds are not robust in AA-forced simulations over 1998–2012. Therefore, the role of AAs in historical climate change remains unclear.

The North Pacific has attracted much attention recently in terms of the effect of AAs. AA forcing might give rise to a weakening of the Aleutian low (Dow et al., 2021; Smith et al., 2016) and a negative phase of the Pacific Decadal Oscillation (PDO) from 1981/1998 to 2012 (Dittus et al., 2021; Smith et al., 2016). Moreover, it has been found that the AA forcing from extratropics can lead to substantial changes in SST in the North Pacific extratropical regions (Diao et al., 2021; Kang et al., 2021; Luongo et al., 2022; Shi et al., 2022). In particular, Shi et al. (2022) have shown the AA-induced patterns at the sea surface based on single-forcing simulations, but the responses in the interior ocean remain unclear. Hence, using the pattern recognition method, we here focus on separating the subsurface patterns of forced ocean temperature responses in the North Pacific from its strong internal variability. The zonal-mean pattern is investigated here to remove the internal variability to some extent.

2. Data and Methods

2.1. Large Ensemble Simulations

The two climate models with large ensemble simulations (more than 10 members) used in our analysis are the Community Earth System Model version 1 (CESM1) and the Canadian Earth System Model version 5 (CanESM5), in which the AA effect can be isolated from their single-forcing ensembles.

For CESM1, the all-forcing large ensemble (LENS, 40 members) and all-but-one-forcing large ensemble (XAER, 20 members) are used (Deser et al., 2020; Kay et al., 2015). Then, we use the method from Deser et al. (2020) to obtain the AA and GHG single-forcing ensemble (20 members each), respectively (Equation 1). We call these derived single-forcing ensembles the CESM1-AER and CESM1-GHG. Each ensemble member is driven by the identical single external forcing but exhibits different internal variability.

$$\mathrm{AER}_{\mathrm{member}} = (\mathrm{XAER}_{\mathrm{member}} - \mathrm{XAER}_{\mathrm{ensmean}}) + (\mathrm{LENS}_{\mathrm{ensmean}} - \mathrm{XAER}_{\mathrm{ensmean}}) \quad (1)$$

CanESM5 has the largest ensemble size in the CMIP6 single-forcing experiments compared with other CMIP6 models. We use 15 members from its historical aerosol-only simulation (hist-aer) and 15 members from the GHG-only simulation (hist-GHG) in which the subsurface variables are available (Swart et al., 2019). Please note that the different experimental designs used in two models, that is, single-forcing versus all-but-one-forcing, can give rise to potential differences in aerosol effects if there are substantial non-linearities in the system. In this study, we show that the results from the two models are quite consistent. The effect of the differences in experimental design merits further careful investigation.

For each model, we also use the preindustrial control simulation (1,800 years in CESM1, 1,000 years in CanESM5) to calculate the PDO index, which is defined as the leading principal component of the area-weighted SST anomalies in the North Pacific (20°N–70°N, 110°E−100°W; Deser et al., 2010). Subsurface temperature is then regressed on the PDO index to obtain the pattern associated with internal variability.

Here, we focus on the upper 1,000 m temperature change in the North Pacific, 0° to 60°N, from 1950 to 2014. We interpolate all the outputs from the two models to a regular $1° \times 1°$ latitude-longitude grid.

2.2. Subsurface Temperature Observations

It is challenging to attribute observed climate variability to AAs on the timescale of one or two decades (Schmidt et al., 2014). Here we use the optimal interpolated EN4.2.2 potential temperature product (EN4-g10 and EN4-c14) from the Met Office Hadley Center and also the recent product from the Institute of Atmospheric Physics (IAP; Cheng et al., 2017) since they cover long periods in the subsurface observations. There are different versions with different methods to correct the bias from expendable bathythermograph (XBT) and mechanical bathythermograph measurements (Cheng et al., 2014; Gouretski & Cheng, 2020; Gouretski & Reseghetti, 2010).

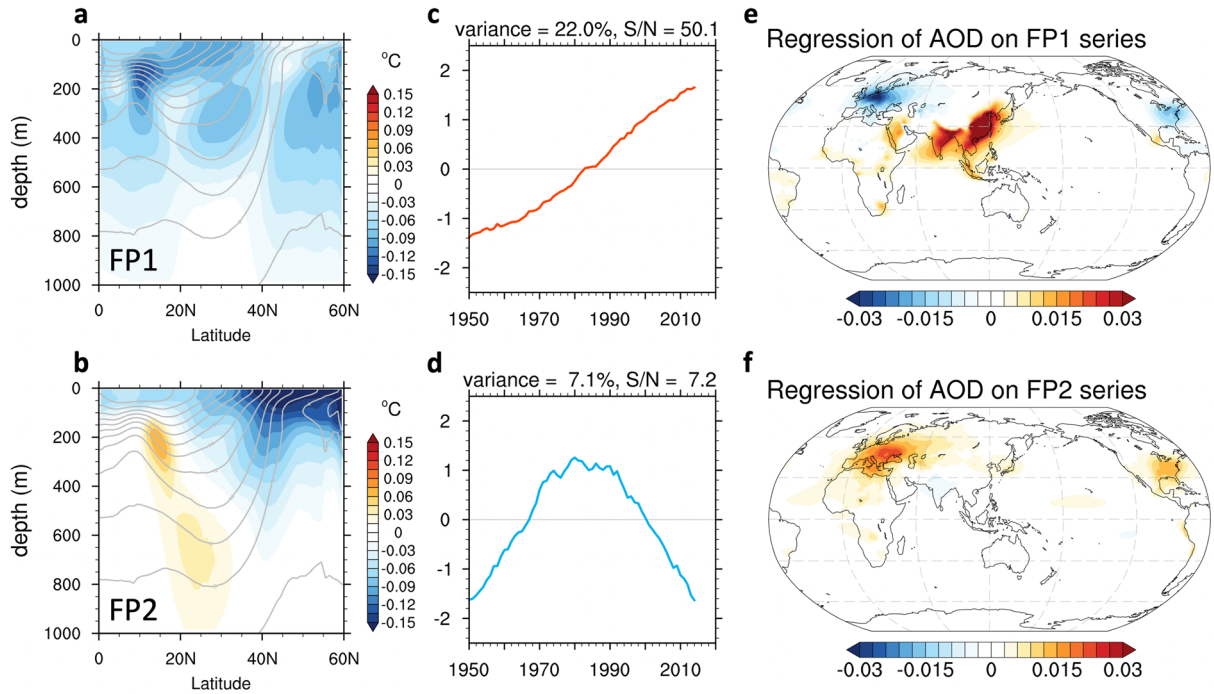

Figure 1. The first two forced patterns (FPs) and time series from CESM1 AER simulations. (a, b) FPs (FP1 and FP2) of North Pacific zonal mean temperature from 1950 to 2014. The mean temperature is shown as contours. (c, d) Standardized time evolution for FP1 and FP2, respectively. (e, f) Regressions of aerosol optical depth on each time evolution.

The data collection, bias correction methods, and gap-infilling methods will create some differences in the objective analyses from these observationally-based datasets. Nevertheless, we focus on their common features extracted from the S/N-maximizing pattern filtering methods (see below). The data are on a $1° \times 1°$ grid from the surface to 1,000 m depth from 1950 to 2020.

2.3. Signal-to-Noise-Maximizing Pattern Filtering

The goal of S/N-maximizing pattern filtering is to extract the anomaly patterns, for which different ensemble members agree on the temporal evolution (Allen & Smith, 1997; Delsole et al., 2011; Déqué, 1988; Schneider & Griffies, 1999; Schneider & Held, 2001; Ting et al., 2009; Venzke et al., 1999; Wills et al., 2018, 2020). This method has been shown to give a clearer forced response than the simple ensemble mean given the limited ensemble member (Wills et al., 2020). In this method, the extracted patterns are associated with the maximization of the ratio of signal (e.g., variance of ensemble mean) to the total variance (from all ensemble members). Full details of this pattern-based method are given in Supporting Information S1 and Shi et al., 2022.

3. Results

3.1. AA-Forced Patterns From Model Simulations

The first two S/N-maximizing patterns of CESM1-AER North Pacific zonal mean temperature anomalies and their time series are shown in Figure 1. Only for these two modes, S/Ns are much greater than 1. For the rest of the modes (not shown), the S/Ns are less than one, and the explained variances are less than 1% without showing a clear long-term temporal evolution. Therefore, we regard the first two patterns as forced patterns (FPs) driven by AA forcing.

FP1 shows a broad subsurface cooling (Figure 1a) with a quasi-monotonic time evolution (Figure 1c). The increasing rate slows down since 2000, which can be explained by the emission regulation. On the other hand, FP2 shows a broad cooling in the upper layer with a much stronger signal in the extratropical region (Figure 1b). The cooling signal mainly penetrates along the steep isothermals in the mid-latitudes. The ventilated thermocline facilitates

the subduction of these cooling signals. In addition, subsurface warming occurs between 10°N–30°N on the equatorward flank of the subtropical gyre, where the meridional gradient of mean ocean temperature is positive. The locations of the negative and positive anomalies relative to the mean pattern indicate that this pattern is associated with the displacement of isotherms due to AA forcing (see Section 3.2). The time series for FP2 exhibits an obvious nonmonotonic evolution, evolving in opposite directions before and after the 1980s. To examine the robustness of the results between models, we calculate the two FPs from CanESM5 AER single-forcing runs (Figure S1 in Supporting Information S1). Its second mode captures a common pattern with a clear nonmonotonic temporal feature. Please note there are some differences between the two models, such as cold anomalies in FP1 are stronger and poleward intensification in FP2 is much more muted in CanESM5, which deserve further investigation.

The regressed pattern of aerosol optical depth (AOD) on FP1 time series (Figure 1e) picks up the geographical transition effect of AA forcing (Shi et al., 2022). This AOD regression pattern shows the transition of the main emissions sites of AA from North America/Europe to East/South Asia, and also the dominant role of the emissions in Asia in the net aerosol increase during this period. The AOD regression pattern on the time evolution of FP2 shows the primary sources of AA forcing located in eastern North America and Europe, regions that underwent early industrial development and then a decline in emission-associated regulations implemented in the mid-1980s. This extratropical AA forcing in FP2 is responsible for the substantial oceanic temperature change in the North Pacific to the north of 30°N (Figure 1b).

Although FP1 explains more variance than FP2, the monotonic increase of GHG forcing can largely offset and even overwhelm the effect of FP1, making the separation of FP1 and GHG signals difficult. Hence, the effect of the nonmonotonically evolving FP2 may be more detectable in the observed historical record. In the following section, we will focus on FP2 and discuss the possible physical mechanisms to explain its characteristic zonal mean pattern.

3.2. Physical Mechanisms Associated With Extratropical Aerosol Forcing

We regress the wind stress anomalies and their curl on the time series of FP2 (Figure 2). The trade winds to the north of the equator and westerly winds are both enhanced relative to the mean wind fields (Figure 2a). This zonal mean wind stress increase gives rise to anomalous Ekman downwelling within 10°–35°N (Figure 2b), driving broadly distributed downwelling wind stress curls in the mid-latitudes (Figure 2d). Consistent with previous studies, a clockwise meridional atmospheric overturning circulation response over the tropics is evident, which is a strong signal of a southward shift of the Hadley Cell (Figure 2f), in response to the NH cooling driven by aerosol forcing. This shift is consistent with the enhanced trade winds to the north of the equator (Figure 2a) and also gives rise to a southward shift of the wind-driven ocean gyres. The southward shift of tropical surface winds and associated enhanced Ekman downwelling together contribute to the subsurface warming on the equatorward flank of the subtropical gyre shown in Figure 1b. It is worth noting that these regression patterns reflect the nonmonotonic evolution of the second mode. Thus, the responses are in the opposite direction after the mid-1980s.

The regression of surface heat flux on the FP2 time series shows a widespread heat loss in the North Pacific (Figure 2c). The heat loss is substantial in the subpolar regions, at similar latitudes to the aerosol sources (Figure 1f), which contributes to the poleward enhanced cooling in the North Pacific (Figure 1b). This poleward enhanced cooling increases the meridional SST gradient, which further affects the tropospheric responses (e.g., Xu & Xie, 2015). The regression of the zonal mean of zonal atmospheric circulation over the North Pacific shows an enhancement of mid-latitude jet streams and a clear poleward shift in the upper troposphere. These atmospheric responses are quite consistent between the two models (Figure S2 in Supporting Information S1). Thus, a poleward shift of the westerly jet can be driven by extratropical aerosol forcing in North America and Europe, likely through the strengthened meridional SST gradient. In this nonmonotonic mode, the responses of the Hadley Cell and N. Pacific jet in the upper troposphere to AA forcing show opposite directions, which is consistent with the result from Diao et al. (2021). They concluded that the shift of the jet stream is attributed to aerosol forcing from South/East Asia, rather than from North America and Europe. In this study, there is a tremendous temperature drop around 40°–45°N (Figure S1b in Supporting Information S1), which is to the north of the jet core (~30°N). Therefore, based on the thermal wind relation, the enhanced SST meridional gradient in North Pacific can produce a strengthening of zonal winds whose maxima are located to the north of the jet core.

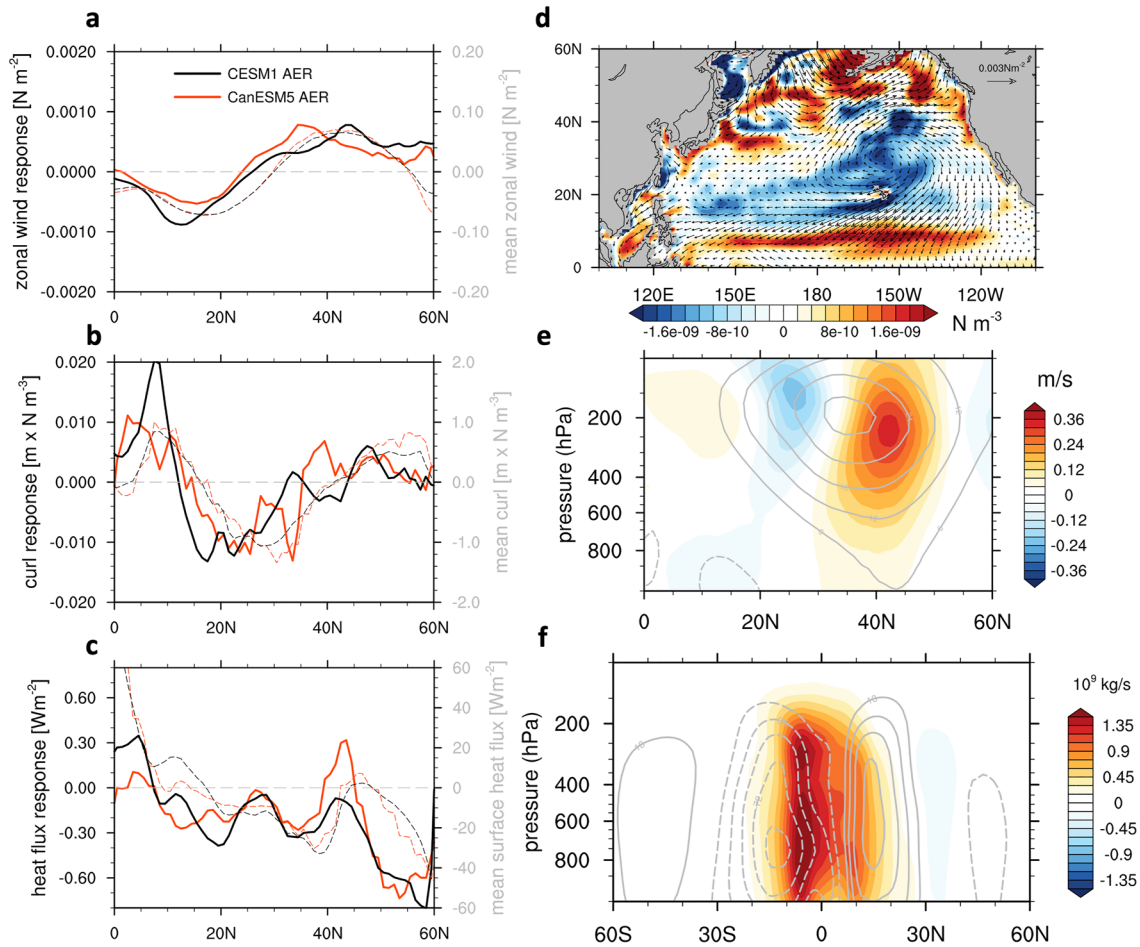

Figure 2. Regressions of various fields on the FP2 time evolution in Figure 1d. (a, c) Regressions of zonal wind stress, wind stress curl, and surface heat flux anomalies on FP2 time evolution from CESM1-AER (black curves) and CanESM5-AER (red curves). (a, c) show the zonal mean of regression and panel b shows the zonal sum of regression of wind stress curl within the North Pacific (0°–60°N, 100°E−100°W). Negative values in panel c denote heat losses from the ocean. The mean fields are shown as dashed curves. (d) Map of regression of surface wind stress (arrows) and wind stress curl (shadings) from CESM1-AER. (e, f) Regression of North Pacific atmospheric zonal mean velocity and global meridional overturning streamfunction, respectively, on FP2 time evolution from CESM1-AER. Positive values in panel f denote clockwise circulations. The corresponding mean fields are shown as contours.

3.3. Results From Observations

As the mid-1980s are the turning point of AA-induced FP2, we calculate the observed trends of North Pacific zonal mean temperature for 1950–1985 and 1985–2020, respectively (Figure 3). The former 36-year trend shows a significant cooling spot in the mid-latitudes, which penetrates mainly along the isotherms (Figures 3a, 3c, and 3e). In addition, the subsurface warm anomalies are found on the equatorward flank of the subtropical gyre, similar to the AA-induced FP2 from the model simulations. For the latter period, the strong warming in the upper layer dominates the overall zonal mean pattern with weaker subsurface cooling on the equatorward flank of the subtropical gyre (Figures 3b, 3d, and 3f). The contrasting trend patterns also appear in the AA single-forcing runs, while the deviations across the ensemble members reflect the impact of background noise (Figures S3 and S4 in Supporting Information S1).

To further show the time evolutions of the observed subsurface temperature, we choose two boxes to calculate the averaged temperature anomalies (Figure 3a). The temperature difference between the two boxes shows a clear nonmonotonic evolution in all three datasets (Figure 3g). The -1xPDO index also exhibits a similar long-term variability but is not able to fully capture the subsurface temporal evolution, especially for the first and last 10 years. We would like to note that this observed PDO can include both the external-forced and internal components. The results from CESM1 simulations for the same boxes are shown in Figure 3h. The GHG effect is relatively

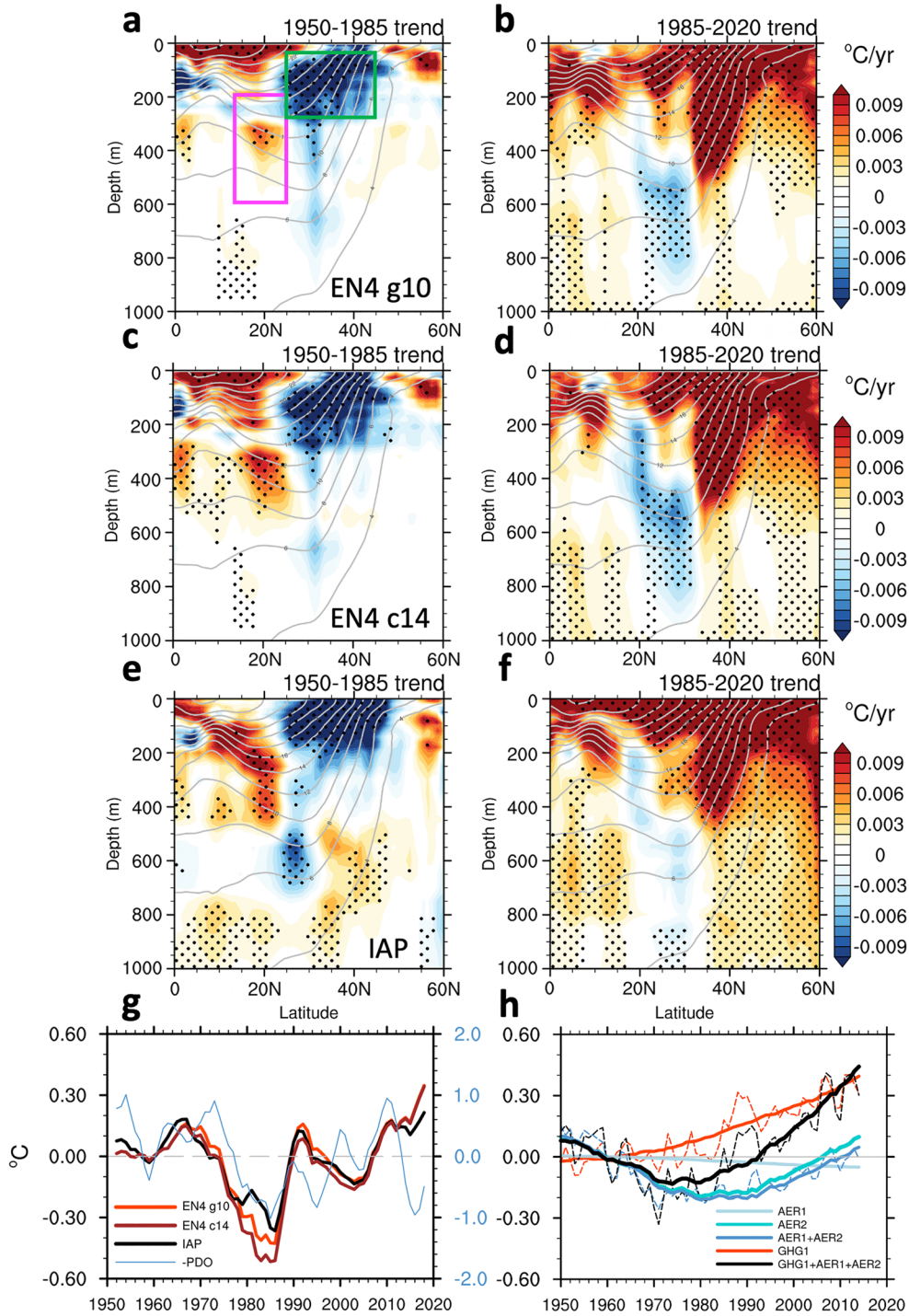

Figure 3. Changes in North Pacific temperature from observations and CESM1 simulations. (a–f) 1950–1985 and 1985–2020 trends of zonal mean temperature from observations. Climatological isotherms are shown as contours. Stippling indicates regions exceeding 95% statistical significance from the two-tailed *t*-test. Panel (g) The 5-year running mean of temperature difference between the average temperature in 25°N–45°N, 50–300 m (green box in panel a and 12°N–25°N, 200–600 m (magenta box) from observations. The 5-year running mean of -1xPDO index from the WMO Regional Climate Center is shown as the blue curve. (h) Temperature difference between two boxes in panel a from CESM1-AER (AER1 and AER2 from FP1 and FP2, respectively) and CESM1-GHG (GHG1 from its first mode). Dashed curves in panel h are the results of a simple ensemble mean of subsurface temperature, <X>.

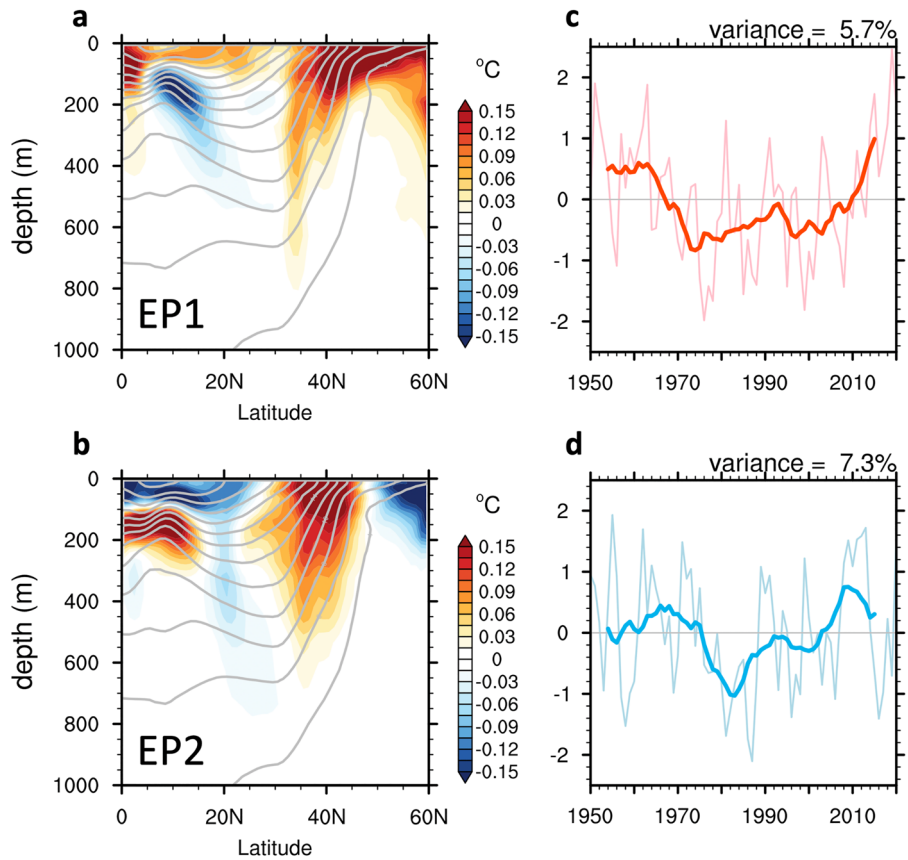

Figure 4. First two extracted patterns and time evolutions from three observational datasets. (a, b) Extracted patterns of North Pacific zonal mean temperature from 1950 to 2020. Climatological isothermals are shown as contours. (c, d) Time evolutions for the extracted patterns. The thick curve denotes the 10-year running mean.

monotonic (red curve in Figure 3h). Importantly, we find that the nonmonotonic feature is predominantly driven by AER2 (reconstructed temperature from FP2 based on Equation S6 in Supporting Information S1; cyan curve in Figure 3h). Hence, the existence of AER2 stemmed from the AA forcing in NH extratropical region can to some extent affect the nonmonotonic trend pattern discovered in observations (Figure 3g).

Although the nonmonotonic feature can be detected, the magnitudes of piecewise trends shown in Figure 3 do not match the AA-induced FP2 well, especially over 1950–1985. To increase the signal-to-noise, we also apply the pattern recognition method to the three observational datasets to extract the common features from them. In this case, it is gridding and bias corrections differences and not internal variability, which is treated as noise. In addition, we expect the observations to reflect both internal variability and all external forcings together.

As we focus on the nonmonotonic feature here, the zonal-mean temperature fields are detrended during 1950–2020 before the pattern recognition analysis. The first mode (EP1) shows strong warming in the upper layer with a poleward amplification and a relatively weak cooling on the southern flank of the subtropical gyre (Figure 4a). The time series of EP1 shows piecewise, long-term trends before and after the 1980s (Figure 4c), which resembles the time series based on the AER2 in Figure 3h. The second extracted mode (EP2) shows a clear tripole pattern (Figure 4b), and the corresponding time series consists of a recognizable multidecadal variability. The S/N ratios in these two modes are much larger than 1. For the remaining modes (not shown), no clear long-term signal is found. The pattern correlation between FP2 and EP1 (Figure 1b vs. Figure 4a) is relatively high ($r = 0.80$ for CESM1, $r = 0.64$ for CanESM5) compared with the correlations between FP2 and the other extracted observed patterns (Table S1 in Supporting Information S1). Hence, EP1 potentially reflects the aerosol fingerprint. In addition, we also conduct the low-frequency component analysis based on the method from Wills et al. (2018), and find the results are quite consistent with the SST responses from their work (Figure S5 in Supporting Information S1).

While it is remarkable that the observed zonal-mean temperature trends in the North Pacific bear similarity to the AA-induced FP2 determined from the model simulations, it is unclear how much the observed multidecadal trends reflect internal variability, especially associated with the PDO. To show the subsurface pattern associated with internal variability alone, we regress the zonal mean temperature from the pre-industrial control run on its PDO index (Figure S6 in Supporting Information S1). The regression shows a tripole pattern that is broadly similar to EP2 from observations. Responses from the control run are more intense in extratropical regions as the PDO index is obtained from 20°N–70°N (Deser et al., 2010). The pattern correlation between the PDO pattern from models and EP2 is relatively high ($r = 0.64$ for CESM1, $r = 0.63$ for CanESM5; see Table S2 in Supporting Information S1). Hence, EP2 is likely to reflect the unforced PDO variability.

4. Summary and Discussion

In this study, we have extracted the influence of anthropogenic forcings on the North Pacific subsurface ocean temperature change since 1950 based on the single-forcing large ensembles of simulations. Despite the confounding effects of internal variability and GHG-forced signals, the AA-forced signals can be extracted using an S/N-maximizing pattern filtering method. Our analysis indicates that aerosol emissions from North America and Europe can cause a clear nonmonotonic time evolution and a characteristic zonal mean pattern of the subsurface ocean temperature within the North Pacific. This response is found in two different climate models with large ensemble simulations, and can be used to understand the AA-induced fingerprints in observations.

Time series analyses, such as that of global/regional mean SSTs, are limited in being able to separate the forced signals from internal noise. The situation is even worse when the observed record is sparse and internal variability is strong and complex. In this study, the ocean subsurface temperature pattern of forced response provides additional information to better characterize the difference between internal modes and changes driven by anthropogenic forcing. For instance, FP2 from the AA simulations is distinct from the PDO-related pattern from the preindustrial run. There are substantial surface heat flux changes in the North Pacific subpolar regions and also tropospheric circulation changes, which leave "fingerprints" in the interior ocean: The increasing surface heat loss in the subpolar regions (prior to ∼1985) leads to strong ocean surface cooling which then subducts into the thermocline. The surface wind change, associated with the equatorward shift of the Hadley cell, strongly affects the temperature change on the equatorward flank of the subtropical gyre. Importantly, after ∼1985, these changes reverse.

Disentangling the roles of internal variability and external forcing in historical climate change remains challenging (e.g., Hua et al., 2018; Qin et al., 2020). We have focused on the nonmonotonic temporal evolution of AAs and their induced zonal mean pattern of subsurface ocean temperature. Here we propose a way to use the obtained FPs from models to compare with the observed changes, although the observed patterns are still open to interpretation. As a caveat, there are some differences between the patterns obtained from models and observations on the regional scale, such as the weaker observed subsurface response at around 500 m, which deserves further investigation. Another useful extension of our work should include the pattern-based fingerprint analysis (e.g., Santer et al., 2018) to understand potential interactions between GHG and AA forcing and how these show up in observations versus models. For the atmospheric circulations, the Hadley cell and jet over the North Pacific shift in opposite directions. The shift of the Hadley cell is attributable to the interhemispheric energy imbalance, and the shift and enhancement of the jet stream are found to be associated with the tremendous temperature change in the North Pacific subpolar region to the north of the jet core. These results are consistent with Diao et al. (2021) but are found to be induced by aerosol emissions from North America and Europe. Rather than the monotonic effect of increasing aerosol emissions widely discussed in previous studies, we show that these atmospheric circulation responses have a clear nonmonotonic feature that further affects ocean responses.

Data Availability Statement

The Community Earth System Model project is supported primarily by the National Science Foundation and the outputs are available from https://www.cesm.ucar.edu/community-projects/lens/data-sets and https://www.earthsystemgrid.org/dataset/ucar.cgd.ccsm4.output.html (Deser et al., 2020; Kay et al., 2015). CanESM5 large ensemble outputs are available on the Program for Climate Model Diagnostics and Intercomparison's Earth System Grid (https://esgf-node.llnl.gov/search/cmip6/) (Swart et al., 2019). IAP data are available at: https://

climatedataguide.ucar.edu/climate-data/ocean-temperature-analysis-and-heat-content-estimate-institute-atmospheric-physics (Cheng et al., 2017). EN4 data are available at: https://www.metoffice.gov.uk/hadobs/en4/ (Good et al., 2013).

Acknowledgments
We gratefully acknowledge the thoughtful and constructive comments from the reviewer Dr. Robert C. Wills and the other anonymous reviewer. This work is supported by U.S. National Science Foundation Grant OCE-2048336. We acknowledge the National Center for Atmospheric Research and the Canadian Centre for Climate Modelling and Analysis producing and making available the model output.

References

Allen, M. R., & Smith, L. A. (1997). Optimal filtering in singular spectrum analysis. *Physics Letters*, *234*(6), 419–428. https://doi.org/10.1016/S0375-9601(97)00559-8

Allen, R. J., Norris, J. R., & Kovilakam, M. (2014). Influence of anthropogenic aerosols and the Pacific Decadal Oscillation on tropical belt width. *Nature Geoscience*, *7*(4), 270–274. https://doi.org/10.1038/ngeo2091

Bonfils, C. J. W., Santer, B. D., Fyfe, J. C., Marvel, K., Phillips, T. J., & Zimmerman, S. R. H. (2020). Human influence on joint changes in temperature, rainfall and continental aridity. *Nature Climate Change*, *10*(8), 726–731. https://doi.org/10.1038/s41558-020-0821-1

Cheng, L., Trenberth, K. E., Fasullo, J., Boyer, T., Abraham, J., & Zhu, J. (2017). Improved estimates of ocean heat content from 1960 to 2015. *Science Advances*, *3*, e1601545. https://doi.org/10.1126/sciadv.1601545

Cheng, L., Zhu, J., Cowley, R., Boyer, T., & Wijffels, S. (2014). Time, probe type, and temperature variable bias corrections to historical expendable bathythermograph observations. *Journal of Atmospheric and Oceanic Technology*, *31*(8), 1793–1825. https://doi.org/10.1175/JTECH-D-13-00197.1

Chung, E. S., & Soden, B. J. (2017). Hemispheric climate shifts driven by anthropogenic aerosol-cloud interactions. *Nature Geoscience*, *10*(8), 566–571. https://doi.org/10.1038/NGEO2988

Dai, A., Fyfe, J. C., Xie, S.-P., & Dai, X. (2015). Decadal modulation of global surface temperature by internal climate variability. *Nature Climate Change*, *5*(6), 555–559. https://doi.org/10.1038/nclimate2605

Delsole, T., Tippett, M. K., & Shukla, J. (2011). A significant component of unforced multidecadal variability in the recent acceleration of global warming. *Journal of Climate*, *24*(3), 909–926. https://doi.org/10.1175/2010JCLI3659.1

Déqué, M. (1988). 10-day predictability of the northern hemisphere winter 500-mb height by the ECMWF operational model. *Tellus A: Dynamic Meteorology and Oceanography*, *40*(1), 26–36. https://doi.org/10.3402/tellusa.v40i1.11780

Deser, C., Alexander, M. A., Xie, S.-P., & Phillips, A. S. (2010). Sea surface temperature variability: Patterns and mechanisms. *Annual Review of Marine Science*, *2*(1), 115–143. https://doi.org/10.1146/annurev-marine-120408-151453

Deser, C., Phillips, A. S., Simpson, I. R., Rosenbloom, N., Coleman, D., Lehner, F., et al. (2020). Isolating the evolving contributions of anthropogenic aerosols and greenhouse gases: A new CESM1 large ensemble community resource. *Journal of Climate*, *33*(18), 7835–7858. https://doi.org/10.1175/JCLI-D-20-0123.1

Diao, C., Xu, Y., & Xie, S. (2021). Anthropogenic aerosol effects on tropospheric circulation and sea surface temperature (1980–2020): Separating the role of zonally asymmetric forcings. *Atmospheric Chemistry and Physics*, *21*(24), 18499–18518. https://doi.org/10.5194/acp-21-18499-2021

Dittus, A. J., Hawkins, E., Robson, J. I., Smith, D. M., & Wilcox, L. J. (2021). Drivers of recent North Pacific decadal variability: The role of aerosol forcing. *Earth's Future*, *9*(12), 1–14. https://doi.org/10.1029/2021EF002249

Dow, W. J., Maycock, A. C., Lofverstrom, M., & Smith, C. J. (2021). The effect of anthropogenic aerosols on the Aleutian low. *Journal of Climate*, *34*(5), 1725–1741. https://doi.org/10.1175/JCLI-D-20-0423.1

England, M. H., McGregor, S., Spence, P., Meehl, G. A., Timmermann, A., Cai, W., et al. (2014). Recent intensification of wind-driven circulation in the Pacific and the ongoing warming hiatus. *Nature Climate Change*, *4*(3), 222–227. https://doi.org/10.1038/nclimate2106

Good, S. A., Martin, M. J., & Rayner, N. A. (2013). EN4: Quality controlled ocean temperature and salinity profiles and monthly objective analyses with uncertainty estimates. *Journal of Geophysical Research: Oceans*, *118*(12), 6704–6716. https://doi.org/10.1002/2013jc009067

Gouretski, V., & Cheng, L. (2020). Correction for systematic errors in the global dataset of temperature profiles from mechanical bathythermographs. *Journal of Atmospheric and Oceanic Technology*, *37*(5), 841–855. https://doi.org/10.1175/JTECH-D-19-0205.1

Gouretski, V., & Reseghetti, F. (2010). On depth and temperature biases in bathythermograph data: Development of a new correction scheme based on analysis of a global ocean database. *Deep-Sea Research Part I: Oceanographic Research Papers*, *57*(6), 812–833. https://doi.org/10.1016/j.dsr.2010.03.011

Hua, W., Dai, A., & Qin, M. (2018). Contributions of internal variability and external forcing to the recent Pacific decadal variations. *Geophysical Research Letters*, *45*(14), 7084–7092. https://doi.org/10.1029/2018GL079033

Hwang, Y.-T., & Frierson, D. M. W. (2013). Link between the double-intertropical convergence Zone problem and cloud biases over the southern ocean. *Proceedings of the National Academy of Sciences*, *110*(13), 4935–4940. https://doi.org/10.1073/pnas.1213302110

Irving, D. B., Wijffels, S., & Church, J. A. (2019). Anthropogenic aerosols, greenhouse gases, and the uptake, transport, and storage of excess heat in the climate system. *Geophysical Research Letters*, *46*(9), 4894–4903. https://doi.org/10.1029/2019GL082015

Kang, S. M., Xie, S., Deser, C., & Xiang, B. (2021). Zonal mean and shift modes of historical climate response to evolving aerosol distribution. *Scientific Bulletin*, *66*(23), 2405–2411. https://doi.org/10.1016/j.scib.2021.07.013

Kay, J. E., Deser, C., Phillips, A., Mai, A., Hannay, C., Strand, G., et al. (2015). The community Earth system model (CESM) large ensemble project: A community resource for studying climate change in the presence of internal climate variability. *Bulletin of the American Meteorological Society*, *96*(8), 1333–1349. https://doi.org/10.1175/BAMS-D-13-00255.1

Kosaka, Y., & Xie, S.-P. (2013). Recent global-warming hiatus tied to equatorial Pacific surface cooling. *Nature*, *501*(7467), 403–407. https://doi.org/10.1038/nature12534

Luongo, M. T., Xie, S., & Eisenman, I. (2022). Buoyancy forcing dominates the cross-equatorial ocean heat transport response to northern hemisphere extratropical cooling. *Journal of Climate*, *35*(20), 1–46. https://doi.org/10.1175/JCLI-D-21-0950.1

Meehl, G. A., Hu, A., Santer, B. D., & Xie, S. P. (2016). Contribution of the Interdecadal Pacific Oscillation to twentieth-century global surface temperature trends. *Nature Climate Change*, *6*(11), 1005–1008. https://doi.org/10.1038/nclimate3107

Oudar, T., Kushner, P. J., Fyfe, J. C., & Sigmond, M. (2018). No impact of anthropogenic aerosols on early 21st century global temperature trends in a large initial-condition ensemble. *Geophysical Research Letters*, *45*(17), 9245–9252. https://doi.org/10.1029/2018GL078841

Qin, M., Dai, A., & Hua, W. (2020). Aerosol-forced multidecadal variations across all ocean basins in models and observations since 1920. *Science Advances*, *6*(29). https://doi.org/10.1126/sciadv.abb0425

Santer, B. D., Po-Chedley, S., Zelinka, M. D., Cvijanovic, I., Bonfils, C., Durack, P. J., et al. (2018). Human influence on the seasonal cycle of tropospheric temperature. *Science*, *361*(6399). https://doi.org/10.1126/science.aas8806

Schmidt, G. A., Shindell, D. T., & Tsigaridis, K. (2014). Reconciling warming trends. *Nature Geoscience*, 7(3), 158–160. https://doi.org/10.1038/ngeo2105

Schneider, T., & Griffies, S. M. (1999). A conceptual framework for predictability studies. *Journal of Climate*, *12*(10), 3133–3155. https://doi.org/10.1175/1520-0442(1999)012<3133:ACFFPS>2.0.CO;2

Schneider, T., & Held, I. M. (2001). Discriminants of twentieth-century changes in Earth surface temperatures. *Journal of Climate*, *14*(3), 249–254. https://doi.org/10.1175/1520-0442(2001)014<0249:LDOTCC>2.0.CO;2

Shi, J.-R., Kwon, Y.-O., & Wijffels, S. E. (2022). Two distinct modes of climate responses to the anthropogenic aerosol forcing changes. *Journal of Climate*, *35*(11), 3445–3457. https://doi.org/10.1175/JCLI-D-21-0656.1

Shi, J.-R., Xie, S.-P., & Talley, L. D. (2018). Evolving relative importance of the southern ocean and north Atlantic in anthropogenic ocean heat uptake. *Journal of Climate*, *31*(18), 7459–7479. https://doi.org/10.1175/JCLI-D-18-0170.1

Smith, D. M., Booth, B. B. B., Dunstone, N. J., Eade, R., Hermanson, L., Jones, G. S., et al. (2016). Role of volcanic and anthropogenic aerosols in the recent global surface warming slowdown. *Nature Climate Change*, *6*(10), 936–940. https://doi.org/10.1038/nclimate3058

Stott, P. A., Tett, S. F. B., Jones, G. S., Allen, M. R., Mitchell, J. F. B., & Jenkins, G. J. (2000). External control of 20th century temperature by natural and anthropogenic forcings. *Science*, *290*(5499), 2133–2137. https://doi.org/10.1126/science.290.5499.2133

Swart, N. C., Cole, J. N. S., Kharin, V. V., Lazare, M., Scinocca, J. F., Gillett, N. P., et al. (2019). The Canadian Earth system model version 5 (CanESM5.0.3). *Geoscientific Model Development*, *12*(11), 4823–4873. https://doi.org/10.5194/gmd-12-4823-2019

Takahashi, C., & Watanabe, M. (2016). Pacific trade winds accelerated by aerosol forcing over the past two decades. *Nature Climate Change*, *6*(8), 768–772. https://doi.org/10.1038/nclimate2996

Ting, M., Kushnir, Y., Seager, R., & Li, C. (2009). Forced and internal twentieth-century SST trends in the North Atlantic. *Journal of Climate*, *22*(6), 1469–1481. https://doi.org/10.1175/2008JCLI2561.1

Trenberth, K. E., & Fasullo, J. T. (2013). An apparent hiatus in global warming? *Earth's Future*, *1*, 19–32. https://doi.org/10.1002/2013EF000165

Venzke, S., Allen, M. R., Sutton, R. T., & Rowell, D. P. (1999). The atmospheric response over the North Atlantic to decadal changes in sea surface temperature. *Journal of Climate*, *12*(8), 2562–2584. https://doi.org/10.1175/1520-0442(1999)012<2562:tarotn>2.0.co;2

Wang, H., Xie, S. P., & Liu, Q. (2016). Comparison of climate response to anthropogenic aerosol versus greenhouse gas forcing: Distinct patterns. *Journal of Climate*, *29*(14), 5175–5188. https://doi.org/10.1175/JCLI-D-16-0106.1

Wilcox, L. J., Highwood, E. J., & Dunstone, N. J. (2013). The influence of anthropogenic aerosol on multi-decadal variations of historical global climate. *Environmental Research Letters*, *8*(2), 024033. https://doi.org/10.1088/1748-9326/8/2/024033

Wills, R. C., Schneider, T., Wallace, J. M., Battisti, D. S., & Hartmann, D. L. (2018). Disentangling global warming, multidecadal variability, and El Niño in Pacific temperatures. *Geophysical Research Letters*, *45*(5), 2487–2496. https://doi.org/10.1002/2017GL076327

Wills, R. C. J., Battisti, D. S., Armour, K. C., Schneider, T., & Deser, C. (2020). Pattern recognition methods to separate forced responses from internal variability in climate model ensembles and observations. *Journal of Climate*, *33*(20), 8693–8719. https://doi.org/10.1175/JCLI-D-19-0855.1

Xu, Y., & Xie, S. P. (2015). Ocean mediation of tropospheric response to reflecting and absorbing aerosols. *Atmospheric Chemistry and Physics*, *15*(10), 5827–5833. https://doi.org/10.5194/acp-15-5827-2015

Geophysical Research Letters

Supporting Information for

Subsurface Temperature Responses to the Anthropogenic Aerosol Forcing in the North Pacific

Jia-Rui Shi*, Young-Oh Kwon, Susan E. Wijffels

Woods Hole Oceanographic Institution, Woods Hole, MA, USA

*Corresponding author address: Jia-Rui Shi, Physical Oceanography Department, Woods Hole Oceanographic Institution, Woods Hole, MA 02543.

Email: jia-rui.shi@whoi.edu

This PDF file includes:

Details about Signal-to-noise-maximizing Pattern Filtering

Figures S1 to S6

Tables S1 and S2

Details about Signal-to-noise-maximizing Pattern Filtering

First, we calculate the zonal mean of the annual mean subsurface temperature in the North Pacific for each ensemble member. The temperature anomalies are calculated relative to the mean of 1950-2014. The obtained temperature anomalies are divided by the temporal standard deviation at each depth for the respective ensemble member to give equal weight to the temporal variability vertically in the following Empirical Orthogonal Function (EOF) analysis, and form the ensemble data matrix **X**, in which the data from each ensemble member are concatenated in the time dimension. We then conduct the EOF analysis on the matrix **X**. The matrix is weighted by the square root of the grid cell area. We define linear combinations of eigenvectors ($\mathbf{a}_k$) from the EOF analysis:

$$\mathbf{u}_k = \left[\frac{\mathbf{a}_1}{\sigma_1} \; \frac{\mathbf{a}_2}{\sigma_2} \; \cdots \; \frac{\mathbf{a}_N}{\sigma_N} \right] \mathbf{e}_k \qquad \text{(S1)}$$

where $\mathbf{u}_k$ is the pattern from the linear combination of N leading EOF eigenvectors. σ_i is the square root of the i-th EOF eigenvalue, and $\mathbf{e}_k$ is a coefficient vector that is determined as that which maximizes the S/N ratio as described below. In this analysis, we pick $N = 50$ retaining around 99% of the total variance.

A corresponding time series $\mathbf{t}_k$ can be defined by projecting $\mathbf{u}_k$ onto the ensemble data matrix **X**.

$$\mathbf{t}_k = \mathbf{X}\mathbf{u}_k \qquad \text{(S2)}$$

To find the robust fingerprint pattern, $\mathbf{u}_k$, we need to find the coefficient vector $\mathbf{e}_k$, which gives the maximum ratio of the ensemble mean signal to the total variance, which can be written as:

$$s_k = \frac{\langle \mathbf{t}_k \rangle^T \langle \mathbf{t}_k \rangle}{\mathbf{t}_k{}^T \mathbf{t}_k} \qquad \text{(S3)}$$

The angle bracket represents the ensemble mean. Thus, the numerator in (S3) denotes the forced signal and the denominator denotes the total variance from all ensemble members.

After plugging (S1) and (S2) into (S3), we get

$$s_k = \frac{\mathbf{e}_k{}^T \left[\frac{\mathbf{a}_1}{\sigma_1} \frac{\mathbf{a}_2}{\sigma_2} \cdots \frac{\mathbf{a}_N}{\sigma_N} \right]^T \langle \mathbf{X} \rangle^T \langle \mathbf{X} \rangle \left[\frac{\mathbf{a}_1}{\sigma_1} \frac{\mathbf{a}_2}{\sigma_2} \cdots \frac{\mathbf{a}_N}{\sigma_N} \right] \mathbf{e}_k}{\mathbf{e}_k{}^T \left[\frac{\mathbf{a}_1}{\sigma_1} \frac{\mathbf{a}_2}{\sigma_2} \cdots \frac{\mathbf{a}_N}{\sigma_N} \right]^T \mathbf{X}^T \mathbf{X} \left[\frac{\mathbf{a}_1}{\sigma_1} \frac{\mathbf{a}_2}{\sigma_2} \cdots \frac{\mathbf{a}_N}{\sigma_N} \right] \mathbf{e}_k} \qquad \text{(S4)}$$

Since the $\mathbf{a}_k$ is the EOF eigenvector of **X**, the covariance in the denominator of (S4) is equal to 1. Therefore, (S4) turns out to be a maximization problem for which s_k and $\mathbf{e}_k$ can be solved.

The S/N-maximizing patterns ($\mathbf{v}_k$), sorted by s_k, are then determined by the regression of the ensemble data matrix **X** onto time-series $\mathbf{t}_k$:

$$\mathbf{v}_k = \mathbf{X}^T \mathbf{t}_k = \left[\sigma_1 \mathbf{a}_1 \; \sigma_2 \mathbf{a}_2 \; \cdots \; \sigma_N \mathbf{a}_N \right] \mathbf{e}_k \qquad \text{(S5)}$$

It should be noted that in this framework, the temporal loadings of the forced patterns are required to be orthogonal, while the spatial patterns are not orthogonal in space. The standard deviation at each depth removed at the beginning is multiplied back on these patterns to obtain the responses with the correct magnitude.

After extracting the forced patterns, we can examine the history of externally forced responses to AAs by constructing its evolution from each forced mode, in which $S/N = s_k/(1 - s_k) > 1$.

$$\langle \mathbf{T} \rangle = \langle \mathbf{t}_k \, \mathbf{v}_k{}^T \rangle \quad \text{(S6)}$$

For instance, when $k = 1$ or $k = 2$, $\langle \mathbf{T} \rangle$ represents the reconstruction of the temperature field due to the first or second forced mode.

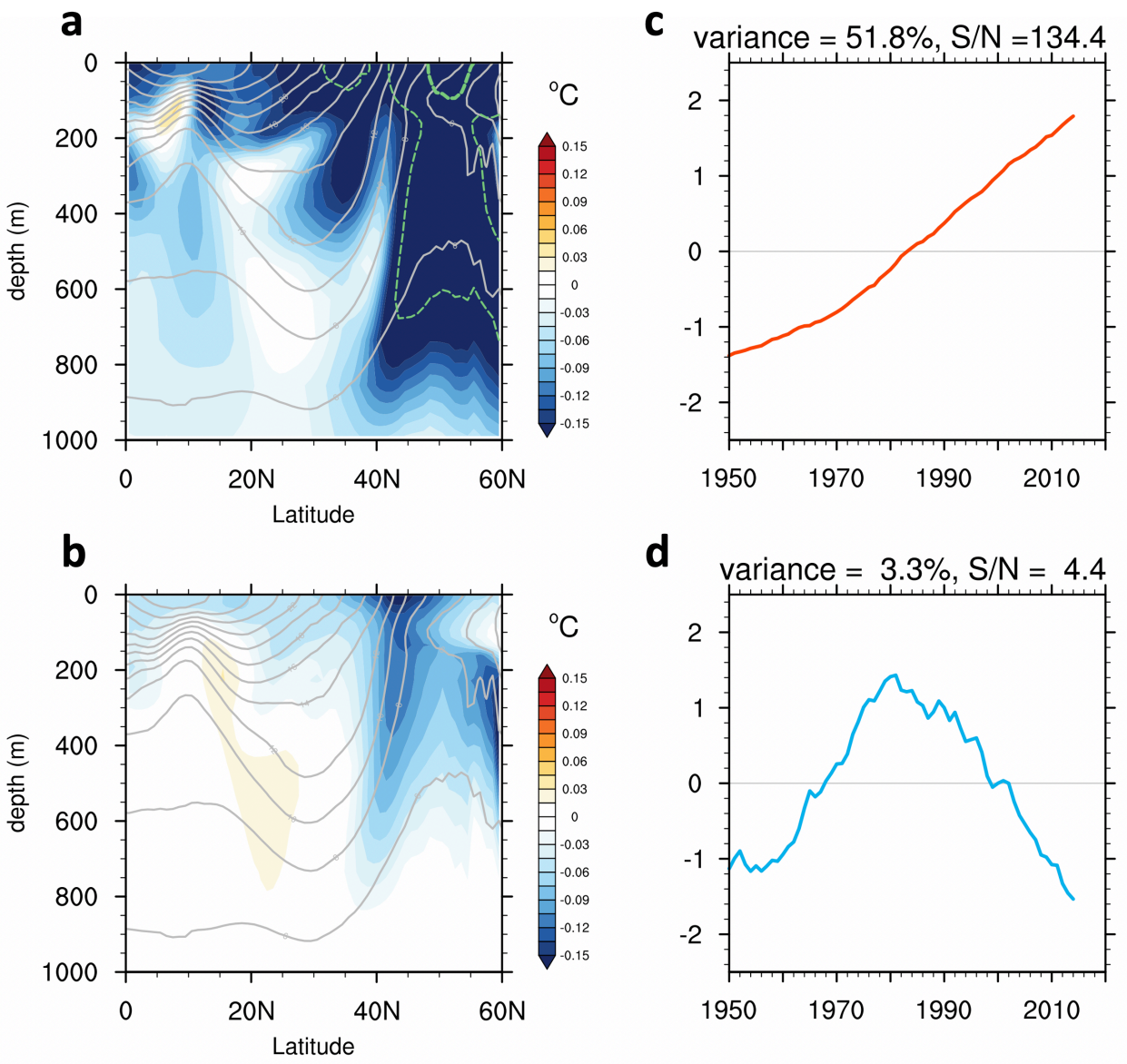

Figure S1. The first two forced patterns and time series from CanESM5 AER simulations. **a-b** First and second forced patterns of North Pacific zonal mean temperature from 1950 to 2014. The mean temperature is shown as contours. In **a**, the thin, green curve denotes the -0.2˚C temperature response, and the thick curve denotes the -0.3˚C temperature response. **c-d** Standardized time evolution for these forced patterns, respectively.

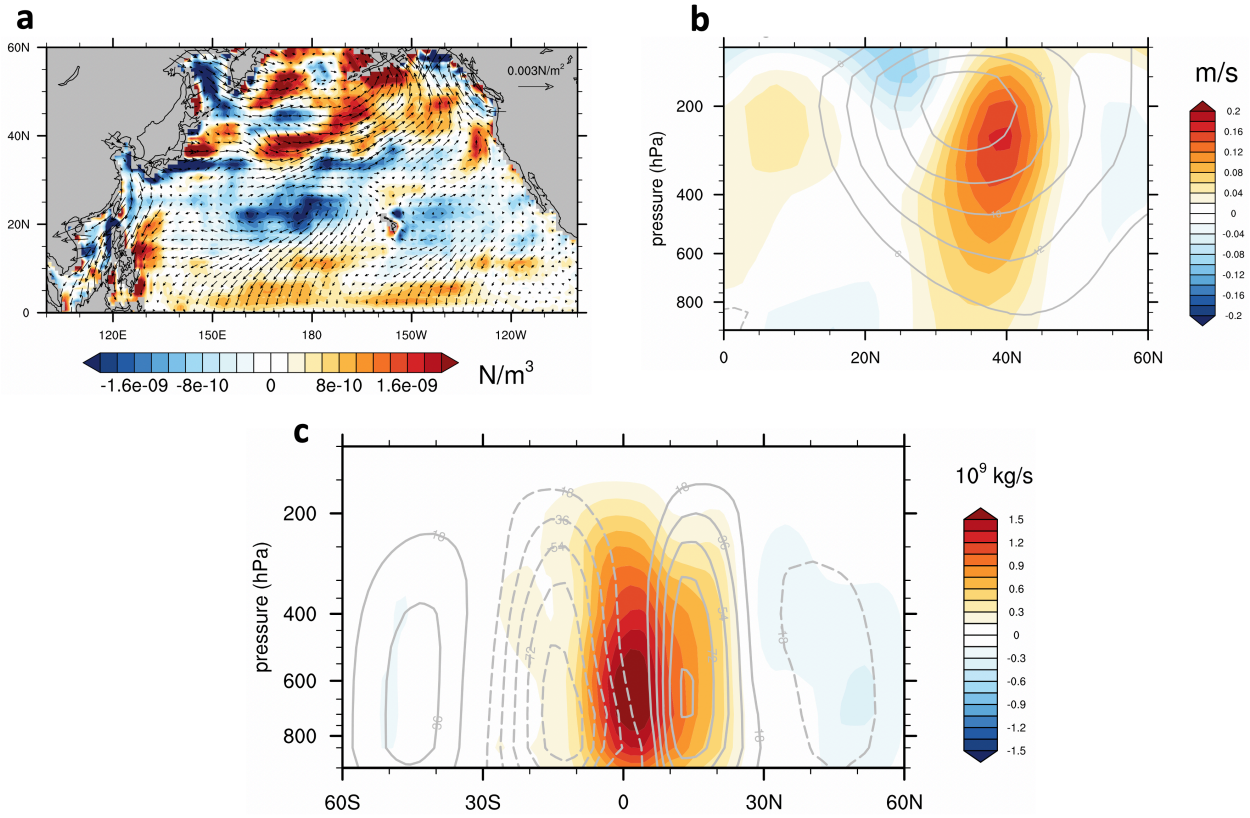

Figure S2. Regressions of various fields from CanESM5 AER on the time evolution of the second forced pattern (FP2) in Figure S1d. **a** Map of regression of surface wind stress (arrows) and wind stress curl (shadings). Negative shadings denote downwelling responses. **b-c** Regression of North Pacific atmospheric zonal velocity and global meridional overturning streamfunction on the time evolution of the FP2, respectively. Positive values in **c** denote clockwise circulations. The corresponding mean fields are shown as gray contours.

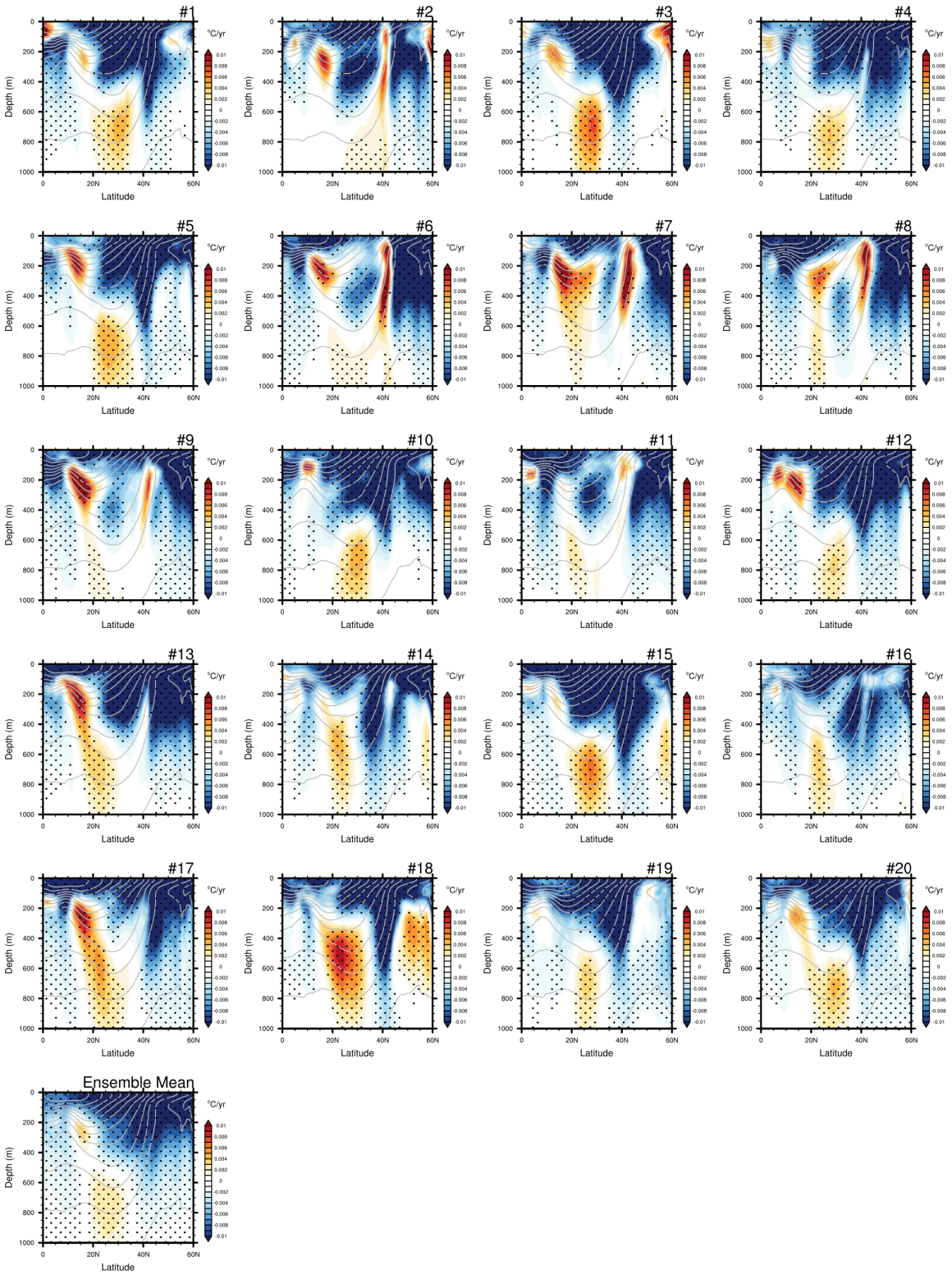

Figure S3. 1950-1985 trends of the zonal-mean North Pacific temperature from individual members and ensemble mean of CESM1-AER. Climatological isotherms are shown as contours. Stippling indicates regions exceeding 95% statistical significance from the two-tailed *t*-test.

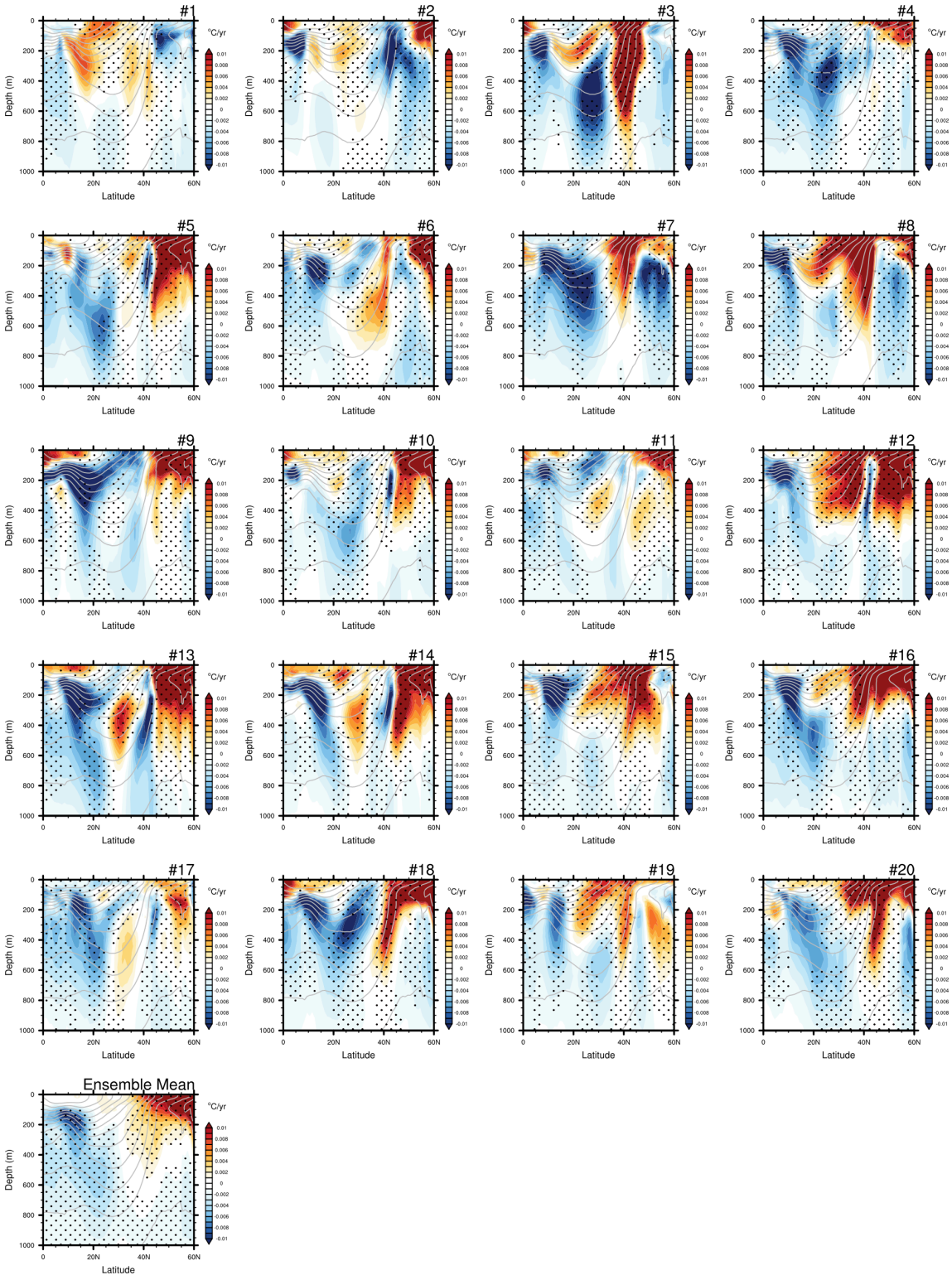

Figure S4. 1985-2020 trends of the zonal-mean North Pacific temperature from individual members and ensemble mean of CESM1-AER. Climatological isotherms are shown as contours. Stippling indicates regions exceeding 95% statistical significance from the two-tailed *t*-test.

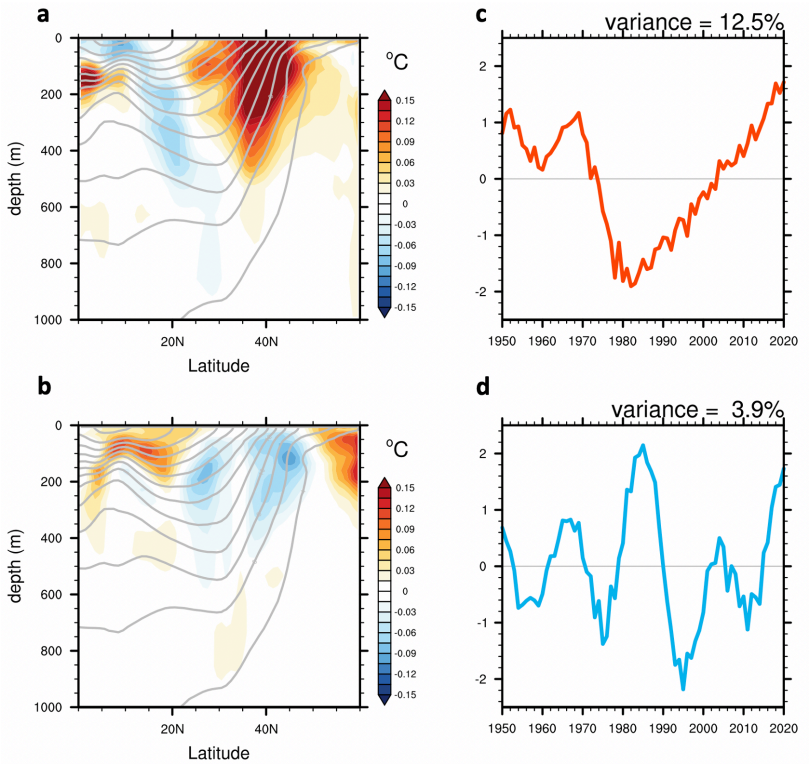

Figure S5. First two leading patterns and the associated time evolutions based on the low-frequency component analysis (15-year lowpass cutoff; Wills et al. 2018) using the mean of three observational datasets. The zonal-mean temperature fields are detrended over 1950-2020 before the low-frequency component analysis, to detect the modes with nonmonotonic temporal evolution.

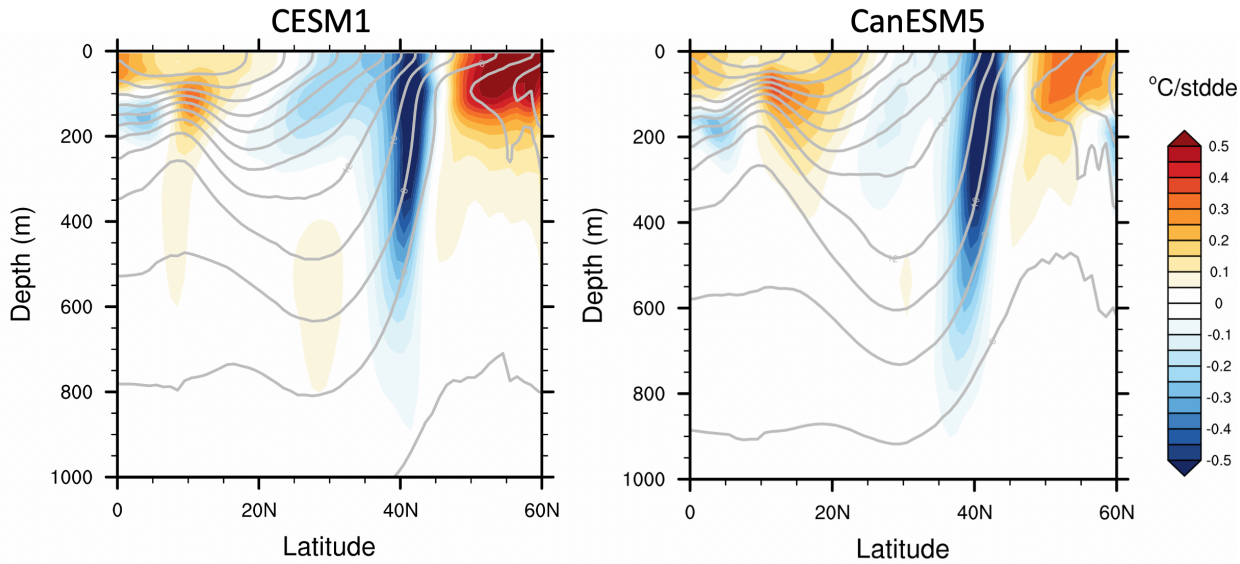

Figure S6. Regression of North Pacific temperature from CESM1 and CanESM5 preindustrial run on the PDO index obtained from the same run. Climatological isotherms are shown as contours.

Table S1. Uncentered pattern correlations (absolute values) between the second forced pattern (FP2) from the two models and the extracted patterns (EPs) from observations.

Observed patterns	FP2 from CESM1-AER	FP2 from CanESM5-AER
EP1	**0.80**	**0.64**
EP2	0.18	0.23
EP3	0.07	0.08
EP4	0.28	0.19
EP5	0.04	0.09

Table S2. Uncentered pattern correlations (absolute values) between the unforced PDO regression pattern from the preindustrial control simulations (PI) and the extracted patterns (EPs) from observations.

Observed patterns	PDO pattern from CESM1 PI	PDO pattern from CanESM5 PI
EP1	0.13	0.25
EP2	**0.64**	**0.63**
EP3	0.15	0.23
EP4	0.39	0.31
EP5	0.01	0.03